Region-specific Brain Targets Drive Circuit Formation and Maturation of Human Retinal Ganglion Cells

Authors: Kang-Chieh Huang[1,2], Han-Yin Jeng[1,3], Qudrat Abdulwahab[1,2], Victoria R. Cuevas[1,2], Eyad Shihabeddin[1,2], Claire Young[1,2], Melody Hernandez[4,5], Jason S. Meyer[4,5], Nicholas M. Tran[3], Melanie A. Samuel[1,2,6,] *

* To whom correspondence should be addressed. Email: msamuel@bcm.edu

Affiliations:

[1] Department of Neuroscience, Baylor College of Medicine, Houston, TX 77030, USA
[2] Huffington Center on Aging, Baylor College of Medicine, Houston, TX 77030, USA
[3] Department of Genetics, Baylor College of Medicine, Houston, TX 77030, USA
[4] Department of Medical and Molecular Genetics, Indiana University School of Medicine, Indianapolis, IN 46202, USA
[5]Stark Neurosciences Research Institute, Indiana University School of Medicine, Indianapolis, IN 46202, USA
[6] Jan and Dan Duncan Neurological Research Institute at Texas Children's Hospital, Houston, Texas, 77030 USA.

Email: msamuel@bcm.edu

Author Contributions: K.H. generated the experimental samples, collected the data, analyzed the data, and assisted in project and experimental conceptualization. H.J., Q.A., V.R.C., E.S., and C.Y. assessed with data analysis. M. H. helped with reagent generation. J.S.M., N.M.T., and M.S. contributed to project conceptualization and supervised the project. M.S. wrote the manuscript

Competing Interest Statement: The authors declare no competing financial interests.

Classification: Biological Sciences/Neuroscience

Keywords: retinal ganglion cell, organoid, synapse, eye-brain wiring, vision

This PDF file includes:

Main Text
Figures 1 to 4
Supplemental Figures 1 to 5

Abstract

Human vision relies on retinal ganglion cells (RGCs), and their connectivity with distinct brain regions enables higher order visual processing. RGCs vary considerably between species, and small model organisms display distinct RGC innervation patterns from that in humans. There is thus a need for robust models of human RGC circuit formation that preserves innervation specificity. Here, we developed an in vitro microfluidics eye-to-brain connectivity model using human pluripotent stem cell (hPSC)-derived RGCs to assess brain region-specific connectivity features. We find that cultured human RGCs segregate their dendrites and axons and display axonal features that align with that of their in vivo human RGC counterparts. The addition of region-specific brain targets to human RGC axons terminals resulted in differential RGC connectivity with distinct retinorecipient brain regions. Increased synapse formation occurred between RGCs and lateral geniculate neurons relative to that with superchiasmatic nucleus neurons, mirroring in vivo innervation differences. Both retinorecipient partners induced the formation of more synapses relative to non-retinorecipient brain target controls. These results suggest that human RGC innervation properties are preserved in culture systems and that human RGCs can differentially sense and respond to retinorecipient targets to control wiring outcomes. These systems may aid in the discovery of human-specific wiring factors for potential therapeutic applications.

Significance Statement

This study presents a novel in vitro model to investigate human retinal ganglion cell (RGC) connectivity, using human pluripotent stem cell-derived RGCs. By modeling human eye-to-brain connections in a microfluidic devise, this system reveals how human RGCs form selective, region-specific synapses with brain areas like the lateral geniculate nucleus and the suprachiasmatic nucleus. The findings demonstrate that human RGCs retain their innervation specificity presences in culture, mimicking in vivo human connectivity patterns. This model provides a powerful tool for understanding the factors controlling human-specific brain wiring, with potential applications in therapies for visual and neurological disorders.

Main Text

Introduction

Retinal ganglion cells (RGCs) are vital conduits for transmitting visual information from the eye to the brain, and their precise connectivity with retinorecipient brain regions is essential for proper visual processing[1,2]. To establish these region-specific connectivity patterns, RGC axons traverse long distances and navigate through various brain circuits. This process involves extending axons within the retina, reaching the optic disc, forming the optic nerve, and projecting either ipsilaterally or contralaterally to synapse with distinct postsynaptic targets.[3] These connectivity patterns differ across brain regions, with some areas receiving dense RGC innervation while others receive sparse inputs from defined RGC types. However, the mechanisms governing RGC axon connectivity upon arrival in a target region remain largely unclear. Two primary models have been proposed to explain this process: the permissive model, where simply reaching a target region is sufficient to promote connectivity, and the instructive model, where RGCs actively respond to region-

specific cues to establish appropriate synapses[2,4,5]. Distinguishing between these alternatives is a critical step toward identifying the molecular signals driving RGC brain innervation.

Understanding how specific postsynaptic regions influence RGC maturation and connectivity is crucial for two main reasons. First, defects in RGC connectivity with their post-synaptic targets underlie many human-specific RGC-related visual disorders, including glaucoma[6,7]. Second, significant differences in RGC diversity and connectivity between humans and mice highlight the necessity of human-specific models[3]. While mice exhibit approximately 47 RGC subtypes[8,9], primates have roughly half that number, with certain RGC types, such as midget cells, dominating the population in primates[10,11]. The abundance of each RGC type also varies between species, with one type of RGC, the midget cell, accounting for ~60% of all primate RGCs[12], while its mouse homolog accounts for only 2% of all mouse RGCs[13]. In turn, midget cell density helps drive human high acuity vision[12,14]. This emphasizes the need to investigate human-specific RGC development and their synaptic connectivity patterns.

Human pluripotent stem cells (hPSCs) have enabled the generation of retinal organoids containing human RGCs (hRGCs), providing a promising model system of human retina visual circuits. However, hRGCs in these systems often lack polarization, fail to extend long axons, and eventually die[15,16]. This death may be due in part to the lack of trophic support from postsynaptic RGC partners[16]. To address these challenges, we previously developed two- and three-dimensional co-culture systems combining retinal organoids with thalamic cultures, demonstrating that hRGC axons can grow and that their survival is enhanced in the presence of innervation targets[16]. Despite these advances, key questions remain: Do hRGCs in vitro develop cellular polarization and structural features

characteristic of maturing RGCs in vivo? And do hRGCs exhibit the same preference for specific retinorecipient targets, such as the lateral geniculate nucleus (LGN) over the suprachiasmatic nucleus (SCN), observed in humans in vivo[17,18]? Finally, how does RGC synapse formation with brain neurons influence the reciprocal maturation of both hRGC and their postsynaptic targets?

To address these gaps, we developed a human eye-to-brain connectivity platform that supports hRGC polarization and integrates region-specific postsynaptic targets, enabling the study of synapse formation and circuit development of human ganglion cells. Using hPSCs from two independent lines, we generated retinal organoids and purified hRGCs, which were cultured in a microfluidic system. This approach facilitated the development of polarized dendrites and axons in hRGCs, including the formation of axon initial segments with in vivo-like molecular composition and organization. hRGCs displayed diverse dendritic morphologies, consistent with advanced maturation. When RGCs axons were cultured with mouse-derived retinorecipient targets, such as the LGN and SCN, hRGCs exhibited increased synapse formation, as evidenced by synapse quantification and circuit tracing. Notably, hRGCs formed more synapses with the LGN versus SCN targets, mirroring in vivo connectivity patterns, and both the LGN and SCN were favored over non-retinorecipient controls. Together, these findings demonstrate that our in vitro human eye-to-brain connectivity model recapitulates in vivo region-specific innervation and suggest that conserved, cell-intrinsic mechanisms drive human RGC connectivity with specific brain regions. This model provides a valuable tool for advancing our understanding of human RGC development and has implications for restoring connectivity in visual disorders and guiding the integration of transplanted cells.

Results

hPSC-derived RGCs develop polarized dendrites and axons

Shortly after their birth, RGCs extend local dendrites that remain near the soma and develop long axons that exit the eye, project through the optic chasm, and establish connections with specific post-synaptic targets in different brain regions[3]. To determine if hRGCs were capable of this distinctive dendritic and axonal polarization, we generated hRGCs from three-dimensional retinal organoids (**Supplemental Figure 1**). We used two hPSC lines that genetically encoded an RGC reporter: the human embryonic stem cell (hESC) H7, which encodes a tdTomato-Thy1.2 reporter, and the human induced pluripotent stem cell (hiPSC) WTC11, which expresses Thy1.2 under the control of the RGC-specific transcription factor Brn3[19]. In both lines, the spatial and temporal generation of retinal neuron subtypes mirrored the developmental stages observed in vivo[20-23], with cycling CHX10 and Ki-67 positive retinal progenitors visible in the outer retina early in development, and laminated, fate committed neurons present later in organoid development (**Supplemental Figure 1B-D**). Human RGCs are among the earliest generated retinal neurons and are born beginning at fetal week four[24]. Similarly, hRGCs (BRN3+) were present in human retinal organoids by culture day 35. The ratio of hRGCs to retinal progenitor cells (CHX10+) increased over time and hRGCs became restricted within the inner retina layer (**Supplemental Figure 1C-D**).

We next examined hRGC neural outgrowth, synapse formation, polarization, and structural complexity of purified RGC cultures over time to assess their maturation in the culture system. To purify hRGCs, we performed enzymatic digestion followed by tagging and isolation using an antibody to the RGC-specific surface protein CD90.2 (Thy1.2) coupled to magnetic beads (**Figure 1A-C**). These generated cultures enriched for hRGCs

for studies of their development and organization (**Figure 1B-D**). We next examined hRGC neural outgrowth, synapse formation, polarization, and structural complexity of purified RGC cultures over time. RGCs formed a low level of synapses with themselves as indicated by staining with synapse marker Synapsin 1 (Syn1) (**Figure 1E**). Staining for the dendritic marker MAP2[25] and the axon initial segment (AIS) marker ankryn G (AnkG)[26] revealed that three weeks post plating, RGCs showed segregated dendrites and axons, with 80% of RGCs showing a defined AIS (**Figure 1F-G**). The percent of hRGCs with AISs did not differ significantly between the hPSC lines ($p = 0.884$, **Figure1G**). AIS structures were further enriched for β-spectrin, a cytoskeletal protein concentrated at the AIS, and for voltage gated sodium channels, which are anchored and clustered at the AIS by βIV-spectrin (**Supplemental Figure 2A**).

To test whether AIS complexity, organization, and structure was conserved with humans RGCs, we stained for several known AIS-enriched proteins and measured their length and distribution. Further, hRGC AIS were between ~30 and 40 um long, with those derived from WTC11 iPSCs showing a small but significant increase in AIS length compared to H7 hPSC-derived hRGCs ($p = 0.007$, **Figure 1H**). These values are similar to those reported for human AIS structures in vivo[27] and in vitro[28]. To assess axon and dendrite segregation, we calculated the hRGC polarity index by taking the intensity ratio between the stain intensity for AISs (AnkG) and the dendritic marker MAP2 immunofluorescence. A polarity index value greater than 1 indicates that the AIS is located toward the axon, while a value less than 1 indicates that the AIS is colocalized with dendrites[29]. hRGCs from both cell lines were highly polarized, with polarity index measures between 2 and 4, and there was no significant difference in polarity between the hRGC groups ($p = 0.806$, **Figure 1I**). We then examined the shape and structure of individual hRGCs via sparse transduction

with a hSyn1-GFP vector and single cell reconstruction (**Figure 1J-K**). The majority of hRGCs had dendrites that clustered around the soma, and a single long axon up to a few millimeters in length (**Figure 1L**). Scholl analysis showed that hRGCs from both lines have a similar level of neurite complexity, with increased dendritic branching near the soma(**Figure 1M**). Together, these data indicate that hRGCs polarize, mature, and develop conserved molecular, structural, and morphological features that mirror human RGCs.

hRGCs polarization is maintained in a microfluidics system

To examine the impact of post-synaptic targets on hRGC connectivity, we first needed to build upon a system in which hRGC axons can be geographically separated from their dendrites. Toward this goal, we utilized a microfluidics system in which hRGC cell bodies are plated in the somatic compartment and the axons are allowed to grow into the distal axonal compartment through microgrooves connecting the chambers (**Figure 2A-B**)[16]. First, we tested the ability of hRGCs to develop and maintain polarization in the microfluidics system. Purified H7 or WTC11-derived hRGCs were seeded into the somatic compartment, and additional brain-derived neurotropic factor (BDNF) and ciliary neurotrophic factor (CNTF, see Material and Methods) were added to the axonal chamber to enhance RGC axon extension into the contralateral axonal compartment[16]. We found that hRGC dendrites remained restricted to the somatic chamber, as indicated by localization of MAP2 positive process confined to this region (**Figure 2C-D**). In contrast, axons were present in the somatic chamber, crossed through the microgrooves, and entered the axonal chamber on the contralateral side as indicated by the presence of SMI-312 in these regions (**Figure 2C-D)**.

As in the standard culture system, hRGCs in the microfluidics device developed highly ordered AISs positive for the AIS marker AnkG, which was present in axons, but not

in dendrites, as indicated by the colocalization with Tubulin III (**Figure 2E**). Quantification revealed that similar to standard hRGC cultures, ~80 % of hRGCs contained an AIS and no significant differences were found between the two lines (*p = 0.537,* **Figure 2F**). The length of the AIS in microfluidics hRGCs mirrored that in the standard culture system, at 28 ± 1.06 µm, though in this case lengths did not vary between hRGCs derived from the two cell lines (*p = 0.723,* **Figure 2G**). hRGCs grown in the microfluidics system were also positive for the AIS enriched proteins β-spectrin and sodium channels (**Supplemental Figure 2B**). Analysis of the polarity index in these cells revealed that hRGC axonal segregation in the microfluidics system was also robust, with values from ~1.5-~3, and no significant difference was observed between the cell lines (*p = 0.104,* **Figure 2H**)

We next asked whether hRGCs had a baseline potential to form synapse proteins by staining for Syn1 and the synaptic vesicle protein SV2. Both proteins could be detected in the somatic and axonal compartments and formed punctate localizations that overlapped with neurites in both chambers (**Figure 2I**). Quantification of the puncta area and puncta density for both markers showed that area and density of SV2 was higher on average than that of Syn1. In both cases, no significant difference was observed between the somatic and the axonal chamber nor were there notable variations in values between the two hPSC lines (**Figure 2J**). Together, these data show that hRGCs from both hPSC lines can be induced to geographically segregate their dendrites and axons, mirroring the arrangement that occurs in vivo, and show proper polarization and AIS formation in these systems.

Retinorecipient targets promote region-specific hRGC connectivity that mirrors in vivo innervation.

During visual system development, RGCs extend axons that specifically and differentially connect with retinorecipient areas and avoid connecting with non-visual targets. In both mice and humans, more RGCs form connections in the LGN, while the SCN is innervated by fewer RGC types[3]. We thus asked whether these distinctions in connectivity were preserved in our in vitro eye-brain connectivity model. We first asked whether presynaptic hRGCs axons could form segregated connections with the postsynaptic neurites of retinorecipient target neurons. Because the defined retinorecipient brain targets cannot yet be generated from hPSC derived-thalamic or diencephalon organoids[30,31], we chose to isolate the developing LGN and SCN from neonatal (postnatal day, P) P1-P3 mice (**Figure 3A**). As a non-retinorecipient control brain region, we chose to isolate the olfactory bulb (OFB). Using cell type-specific markers, we validated that cultured mouse LGN, SCN and OFB retained the normal distribution of cell types and area-specific markers observed in these regions in the intact brain. The bulk of cells in these cultures were neurons, as indicated by staining for MAP2 (~70-85%), and microglia (IBA1) and astrocytes (GFAP) were also present at expected ratios (**Figure 3B-C**). In addition, a subset of cultured LGN neurons were positive for FOXP2, a transcription factor enriched in a subset of LGN neurons in vivo[32,33], while a subset of SCN cultures were positive for vasoactive intestinal polypeptide (VIP), neurons essential for circadian entrainment[34,35] **(Supplemental Figure 3A-B**). These data are consistent with the idea that post-synaptic cellular identity is preserved in LGN and SCN cultures.

We next asked whether hRGCs could form connections with postsynaptic targets. To begin to assess this, we focused on H7-derived hRGGs as there were few significant differences between hRGCs from both lines, and the H7 line had the advantage of carrying the tdTomato reporter. H7-derived hRGCs were plated in the somatic chamber of the

microfluidics system and allowed to extend axons, followed by the addition of LGN, SCN, or OFB cells into the axonal chamber. We found that in all cases, tdTomato hRGC axons anatomically colocalized with MAP2 positive postsynaptic target neurites, suggesting the potential for connectivity (**Supplemental Figure 4**). We then assessed connectivity directly using retrograde viral tracing (**Figure 3**). LGN, SCN, or OFB cells were isolated, dissociated, infected with AAV-Retro-GFP[36], and then washed extensively to remove any excess virus. We validated that the percentage of post-synaptic neurons infected by AAV-Retro GFP did not differ between brain regions ($p = 0.9$ **Figure 3E and I**). Infected postsynaptic cells were then plated in the axonal chamber of microfluidics devices in which hRGCs had been established, and retrograde labeling of hRGC somas was analyzed 10 days after postsynaptic neuron plating (**Figure 3F-H**). The number of hRGC somas that were labeled by retrograde tracing was elevated in presence of LGN and SCN postsynaptic targets relative to OFB non-retinorecipient post-syanptic targets (**Figure 3J**). These data suggest that presynaptic hRGCs axons can form properly orientated connections and that hRGCs may preferentially connect with retinorecipient neurons in this microfluidics model of eye-brain wiring.

To validate and extend these findings, we asked whether the area and number of synapses formed between hRGCs differed between LGN, SCN, and OFB. As above, hRGCs were grown in microfluidics chambers and allowed to extend axons, followed by the addition of LGN, SCN or OFB targets (**Figure 4A**). Ten days after post-synaptic target addition, Syn1 was used to label and quantify the area and number of synapses formed on tdTomoato positive RGC axons. We found that hRGCs formed significantly more Syn1 positive puncta that were increased in area when LGN neurons were added to the axonal compartment relative to all three alternative conditions: hRGCs alone (2 fold increase, $P <$

0.0001), the addition of SCN cells (1.7 fold increase, P = 0.0005), and the addition OFB cells (2.05 fold increase, P < 0.0001, **Figure 4B-C**). We also assessed Syn1 puncta number and area in the somatic compartment as one read out of the impact of postsynaptic neurons on presynaptic neuron maturation. We found that the addition of either LGN or SCN neurons significantly increased the area ($P \leq 0.001$) and number ($P \leq 0.01$) of Syn1 positive puncta in the hRGC somatic compartment relative to either hRGCs alone or the addition of OFB cells (**Figure 4D-E**). Further, when LGN, SCN, and OFB neurons were exposed to hRGC axons, post-synaptic neuron maturation improved as measured by the number of postsynaptic synaptic neurons that contained AnkG positive axon initial segments (**Supplemental Figure 5**). Together with our retrograde tracing experiments, these data suggest that in vivo distinctions in visual system connectivity can be preserved in our in vitro eye-brain connectivity system. Both retinorecipient targets enhance hRGC Syn1 somatic levels and improve postsynaptic neuron maturation.

Discussion

To understand human neural development and disease so that effective therapies can be developed, it is important to have robust human models of neural connectivity that preserve cell identity, wiring patterns, circuit organization, and specificity. In this study, we developed an in vitro microfluidic model of eye-to-brain connectivity using hPSC-derived RGCs to evaluate connectivity characteristics specific to different postsynaptic brain regions. We found that two different hPSC lines can give rise to hRGCs that develop polarized dendritic and axonal structures when cultured alone and when plated in microfluidics systems. Axons grew long distances (>450 um), effectively targeted the distal chamber, and formed distinct axon initial segments that were of similar lengths and

organization to that observed in human samples in vivo. Using retrograde viral tracing, we showed that hRGCs generated connections with mouse retinorecipient postsynaptic targets. Further, synapse formation was elevated between hRGCs and LGN targets compared to SCN partners and controls, mirroring in vivo patterns of innervation. These findings indicate that the innervation properties of human RGCs are maintained in culture systems, allowing these cells to selectively recognize and respond to retinorecipient targets. Such systems could be valuable in identifying human-specific wiring factors for potential therapeutic interventions.

There are several advantages to our model of eye-to-brain connectivity. First, it has the capacity to enable pre and postsynaptic assessments of human RGCs for both normal development and in the context of genetic disease variants. This is an important advancement because while other studies have shown that retinal organoids can give rise to RGCs, these cells die at later stages of differentiation[15,16]. Further, hRGC axons do not develop well in organoids and are unable exit organoids under standard preparations, precluding the ability to study axon initiation, extension and connectivity[15,16]. While several factors likely contribute to hRGC loss in these systems, one factor may be the lack of neurotrophic support from postsynaptic partners[37]. Our model overcomes these limitations by providing hRGCs with appropriate postsynaptic partners. A second advantage of our system is the use of distinct retinorecipient targets derived from mice that preserve region-specific neural populations, allowing for the examination of differential innervation properties. This approach is particularly valuable, as current human thalamic culture systems do not facilitate the derivation of LGN versus SCN cell types. Finally, our microfluidics system permits direct assessment of directional connectivity, synapse number, and synapse size, which can prove challenging in other approaches. This model provides

an alternative to human assembloid circuits[16] and related systems[38-40] that may be better suited for questions regarding brain region specific synapse specificity.

How might human eye-brain connectivity models be used to understand RGC axonal guidance and postsynaptic interactions? In the developing eye, RGC axons exit the eye, form the optic nerve, determine whether to project ipsilaterally or contralaterally at the optic chiasm, and form connections with specific brain targets. Several repulsive and attractive cues help guide this process, including Eph receptors and ephrins (reviewed in[41]). In addition, the adult SCN expresses slit/robo inhibitory cues that prevent innervation from RGCs[42]. It is interesting to envision alternative forms of the system we describe that could be used to model various aspects of this process. These include: 1) providing cues in alternative chambers, 2) allowing axons to 'choose' between different retinorecipient targets, or 3) modeling competitive axon refinement between 'ipsilateral' and 'contralateral' RGC inputs. In addition, this system may be suitable for uncovering brain region specific factors that provide RGC trophic support. For example, our data are consistent with the idea that postsynaptic partners enhance RGC maturation as the addition of retinorecipent targets but not a non-recipient control brain region improved Syn1 positivity in the RGC somatic compartment. In line with this idea, retrograde neurotrophic support from postsynaptic neurons can also directly enhance RGC survival both in development[43-45] and in disease conditions[46,47]. Lastly, the capability to examine distinct post-synaptic targets has the added advantage of providing a system to study RGC influence on brain neuron maturation. For example, RGC axons can provide a scaffold for LGN maturation via activity dependent regulation of astrocytes and their ability to produce the inhibitory neuron recruiting molecule fibroblast growth factor 15[48]. In future studies, it will be interesting to assess the long-term

effects of individual postsynaptic targets in modulating RGC persistence and resilience, and conversely to assess the impact of RGCs on brain neuron maturation.

Finally, the system we describe has potential implications and utility for the study of retinal and other neurodegenerative diseases. For example, human patient samples could be used to grow hRGCs to model individual diseases and phenotypes[49,50]. This is particularly important because the expression of proteins linked to genetic glaucoma risk in humans (e.g. such as *OPTN*[51], *GAS7*[52], *SIX6*[53], and *MAP3K1*[54]) may not be well conserved in mouse RGCs. This is supported by findings that genetic models of human glaucoma risk factors, like the E50K mutation in OPTN, result in only mild phenotypic changes in mice[55], despite causing severe disease in humans[56]. In addition, our system permits compartmentalized study and manipulation of dendritic versus axonal hRGC outcomes. This is of relevance to diseases such as glaucoma, in which both RGC dendrites and axons degenerate, and these processes may occur via different mechanisms[6,7]. A further advantage of the compartmentalized system we describe is the ability to selectively modulate axons as they exit the somatic chamber and before they enter the axonal chamber. This may more closely mimic glaucoma induced modulation of RGCs axons as they exit the eye passing through the lamina cribosa, which is thought to be the initial site of insult human glaucoma[57]. Another important application will be the discovery of human molecular pathways that determine brain-region specific connectivity outcomes and resiliency. The potential for this system as a discovery platform is particularly encouraging given that RGC axons formed a significantly higher number Syn1 positive puncta with the LGN compared to the SCN, mirroring the higher number of RGCs that innervate the LGN versus SCN in primates[17,58]. Given these results, it will be interesting to determine whether RGCs that innervate LGN versus SCN postsynaptic targets are differently resilient to

disease-related insults. Such approaches may provide new therapeutic opportunities for precise intervention in the progression of retinal and other neurological diseases.

Materials and Methods

hPSCs maintenance and retinal organoid differentiation

Two hPSC lines, human embryonic stem cell line H7 and human induced pluripotent stem cell line WTC11, were used in this manuscript. H7 has been previously genetically engineered with an RGC tdTomato reporter and Thy1.2 antigen at the BRN3b locus as described (PMID: 29024560) (BRN3:tdTomato:Thy1.2)[19], while WTC11 was edited using similar approaches to genetically introduce the Thy1.2 antigen without tdTomato at the BRN3b locus (BRN3:Thy1.2). hPSCs were maintained in matrigel- (Fisher Scientific, cat# 8774552) coated plates with mTeSR™ Plus (StemCell Technologies, cat# 100-0276) medium. hPSCs were split every 4-5 days by Dispase (2 mg/mL, Life Technologies, cat# 17105041) as described previously[50,59-61].

Methods for generating retinal organoids have been described previously [50,59-61]. In brief, to generate retinal organoids, the 80% confluence of hPSCs were enzymatically dissociated by Dispase for 10 min in a 37°C incubator. The dissociated clump hPSCs were plated on low adherent plates in mTeSR1 (StemCell Technologies, cat# 85850) and Neuronal Induction Medium (NIM, composed of DMEM/F12(1:1) supplement with 1X N2 supplement, MEM-NEAA and 2 μg/ml heparin) with a ratio of 3:1 on day 0 and gradually transitioned to full NIM on day 3 (the mTeSR1 to NIM is 1:1 on day 1 and 1:3 on day 2) to induce embryonic bodies. On day 6, change the medium to full NIM supplement with BMP4 (50 ng/mL, R&D Systems, cat# 314-BP-050) to enrich retinal organoids. The embryonic bodies were plated on the 6-well plate on day 8 with a density of 100-200 embryonic bodies

per well in NIM with 10% FBS to promote cell adherence. Replace a fresh NIM the next day, and the medium was changed every 2-3 days with fresh NIM. On day 16, the loosely attached rosettes were mechanically lifted by a P1000 tip, and transferred the colonies to low adherent plates to allow retinal organoid specification in Retinal Differentiation Medium (RDM, composed of DMEM/F12(3:1) supplemented with 1X B27, MEM-NEAA, and Anti-Anti) and replace half-fresh RDM every 2-3 days until the time point was reached. The RDM was supplemented with 1X GlutaMAX since day 20, and starting supplemented with 1% FBS on day 20, 5% FBS on day 25, 10% FBS on day 30. From day 35, retinal organoids were fed with RDM supplement with 10% FBS, 1X GlutaMAX, and 100 μM Taurine.

RGC purification from retinal organoids

Methods for RGC isolation and purification from retinal organoids have been described previously with slight modifications[19,50]. Collected day 45-60 retinal organoids in a 15 mL conical tube, washed by warm DMEM/F12 once, and incubated with the dissociate solution in the 37°C water bath for 20 min (agitate the tube every 5 min). The dissociate solution is composed of AccuMAX (Life Technologies, cat# 00-4666-56), Papain (16 unit/mL, Worthington Biochemical Corporation, cat# LS003126), DNase I (Sigma, cat# D4527), 5.5mM L-cysteine (Sigma, cat# C1276), and 100X HEPES (Life Technologies, cat# 15630080), and activate the solution in 37°C water bath for at least 15 min before used. After 20 min incubation with retinal organoids, remove the dissociate solution and add RDM supplement with 10 mg ovomucoid inhibitor (Worthington Biochemical Corporation, cat# LS003087) and 10 mg BSA. Pipetting and mechanically dissociating retinal organoids to single cells using a P1000 pipette and straining by 30 μm filters (Miltenyi, cat# 130-041-407). Centrifuge the dissociated cells and wash them with RDM once before incubating the

cells with CD90.2 microbeads (Miltenyi, cat# 130-121-278), followed by a MACS cell separation kit[19]. 30-50k purified RGCs were plated on a poly-D-Lysine (Life Technologies, cat# A3890401) and Laminin (Life Technologies, cat# 23017015)-coated 12 mm coverslip in Neurobasal A medium (Life Technologies, cat# 10888022), supplement with 1X N2, B27, GlutaMAX, Anti-Anti, 20 ng/mL BDNF, and 20 ng/mL GDNF. The medium was changed every 3-4 days and maintained for up to 4 weeks.

RGC and co-culture with brain postsynaptic targets in microfluidic devices

The setup of microfluidic devices (Xona Microfluidics, cat# XC450) follows manual instructions two days before plating RGCs. On day 1, the microfluidic device was treated with XC Pre-Coat solutions and coated with poly-D-lysine overnight in a 4°C fridge. On day 2, the device was washed with PBS three times and coated with Laminin overnight in a 37°C incubator. 50-100k purified RGCs were plated in the device on the next day in Neurobasal-A medium. An extra 50-100 µl volume is added in the somatic chamber to maintain the fluidic physical isolation while supplementing 50 ng/mL BDNF and 50 ng/mL CNTF in the axonal chamber to induce axon outgrowth[16]. The medium was changed every 2-3 days and maintained for up to 4 weeks. To set up co-culture with brain targets, 80k RGCs were plated in the somatic chambers for 10 days, following 70-80k brain targets in the axonal chambers for an additional 10 days of co-culture before analysis.

Animal model and primary cultures

Experiments with mice were carried out in accordance with the recommendations in the Guide for the Care and Use of Laboratory Animals of the NIH under protocols approved by the BCM Institutional Animal Care and Use Committee. C57BL/6J strain (JAX 000664)

or CD1 wildtype mice (obtained from Charles River Laboratories) were used in this study. To establish the primary cultures from retinorecipient brain targets, dissected fresh LGN, SCN, and olfactory bulb tissue from P0-P3 mice and collected in the cold DMEM/F12 medium. Incubate the tissue with the papain solution (DMEM/F12 medium composed of 16 unit/mL papain, DNase I, L-cysteine, and 100X HEPES) in the 37°C water bath for 20 min (agitate the tube every 5 min). Remove the papain solution and quench by DMEM/F12 supplement with 10 mg ovomucoid inhibitor and 10 mg BSA. Pipetting and mechanically dissociating the brain tissue to single cells using a P1000 pipette and straining by 70 μm filters. 50k cells were plated in poly-d-lysine and laminin-coated 12 mm coverslips, and 70-80k cells were plated in axonal chamber of microfluidic devices in the Neurobasal-A medium supplement with growth factors as mentioned above. The medium was changed every 3-4 days and maintained for up to 10 days.

Viral transsynaptic tracing

AAV viruses were packaged with pAAV-Syn1>EGFP:WPRE (VectorBuilder, cat# VB240311-1387gfy). For retrograde tracing, brain target cells (LGN, SCN, or olfactory bulb) were infected with AAV2-retro-Syn1>EGFP:WPRE at an MOI of 1 x 10^6. All the AAV viruses were packaged from VectorBuilder. Cells were infected in the 96-well U bottom plate and incubated in the 37°C incubator for an hour. After viral infection, the cells were washed with warm DMEM/F12 three times to remove any residual AAV from the medium. Cells were resuspended by Neurobasal-A medium and plated in the microfluidic devices. To ensure the proper viral transsynaptic tracing and no residual AAV in the culture medium, the medium from the last wash was collected and put in the microfluidic device as a negative control.

Immunocytochemistry

Cells were fixed with 4% paraformaldehyde at room temperature for 30 min, followed by blocking with 10% donkey serum, 5% BSA, and 0.2% Triton-X in a PBS solution for an hour. For staining axon initial segment proteins, the cells were fixed with 2% paraformaldehyde at room temperature for 15 min instead. Diluted the primary antibodies in 5% donkey serum, 2.5% BSA, and 0.1% Triton-X in the PBS solution and incubated overnight at 4°C fridge. Primary antibodies and their dilute factors are anti-mouse CHX10 (Santa Cruz, cat# sc-365519, 1:200), anti-rabbit Ki67 (Invitrogen, cat# MA5-14520, 1:250), anti-goat BRN3 (Santa Cruz, cat# SC-6026, 1:200), anti-goat tdTomato (Origene, cat# AB8181-200, 1:500), anti-chicken MAP2 (Abcam, cat# ab5392, 1:2000), anti-rabbit MAP2 (Proteintech, cat# 17490-1-AP, 1:100), anti-rabbit Synapsin-1 (Millipore-Sigma, cat# AB1543, 1:200), anti-rabbit Synapsin-1 (Cell Signaling, cat# 5297, 1:200), anti-chicken GFP (Abcam, cat # ab13970, 1:2000), anti-goat IBA1 (Abcam, cat# ab5076, 1:100), anti-mouse GFAP (Millipore-Sigma, cat# G3893, 1:200), anti-sheep FOXP2 (R&D system, cat# AF5647, 1:200), anti-rabbit NeuN (Proteintech, cat# 26975-1-AP, 1:200), anti-rabbit VIP (Immunostar, cat# 20077, 1:1000), anti-mouse SMI-312 (BioLegend, cat# 837904, 1:500), anti-rabbit TUBB3 (BioLegend, cat# 802001, 1:1000), anti-mouse Tau (Millipore-Sigma, cat# MAB3420, 1:200), anti-mouse Ankyrin-G (NeuroMab, cat# 75-146, 1:200), anti-rabbit βIV-spectrin (from Rasband lab, 1:200), and anti-mouse Pan sodium channel (NeuroMab, cat# 75-407, 1:200). On the following day, the cells were washed with PBS three times, followed by incubating them with secondary antibodies and DAPI (Cell Signaling, cat# 4083, 1:1000) in 5% donkey serum, 2.5% BSA, and 0.1% Triton-X in the PBS solution for an hour at room temperature. The cells were washed with PBS three times and stored either in

mounting media (ProLong Gold Antifade Mountant, Life Technologies, cat# P36930) or PBS (for microfluidic devices). The images were acquired using Olympus Fluoview FV1200 confocal microscope, ZEISS LSM 880 confocal microscope, or ZEISS Axio Observer. All images were processed in Fiji (ImageJ).

The following antibodies were used in our analyses:

Antibody	**Type**	**Source**	**Catalog Number**	**ICC Dilution**	**Identifier**
CHX10 (E-12)	mouse monoclonal	Santa Cruz	sc-365519	1:200	RRID:AB_10842442
MAP2	Chicken polyclonal	Abcam	ab5392	1:2000	RRID:AB_10842442
MAP2	Rabbit polyclonal	Proteintech	17490-1-AP	1:100	RRID:AB_2137880
SMI-312	mouse monoclonal	BioLegend	837904	1:500	RRID:AB_2566782
Synapsin-1	Rabbit polyclonal	Millipore-Sigma	AB1543	1:200	RRID:AB_2200400
Synapsin-1	Rabbit monoclonal	Cell Signaling	5297	1:200	RRID:AB_2616578
VIP	Rabbit polyclonal	Immunostar	20077	1:1000	RRID:AB_572270
BRN3	Goat polyclonal	Santa Cruz	SC-6026	1:200	RRID:AB_673441
FOXP2	Sheep polyclonal	R&D system	AF5647	1:200	RRID:AB_2107133
IBA1	Goat polyclonal	Abcam	ab5076	1:100	RRID:AB_2224402
GFAP	mouse monoclonal	Millipore-Sigma	G3893	1:200	RRID:AB_477010
NeuN	Rabbit polyclonal	Proteintech	26975-1-AP	1:100	RRID:AB_2880708

Ki67	Rabbit Monoclonal	Invitrogen	MA5-14520	1:250	RRID: AB_10979488
tdTomato	Goat polyclonal	Origene	AB8181-200	1:500	RRID:AB_3206272
GFP	Chicken polyclonal	Abcam	ab13970	1:2000	RRID:AB_300798
TUBB3	Rabbit Polyclonal	BioLegend	802001	1:1000	RRID:AB_2564645
Tau	Mouse Monoclonal	Millipore-Sigma	MAB3420	1:200	RRID:AB_10947848
Ankyrin-G	Mouse Monoclonal	NeuroMab	75-146	1:200	RRID:AB_2877524
βIV-spectrin	Rabbit polyclonal	Rasband lab		1:200	RRID:AB_2315634
Pan sodium channel	Mouse Monoclonal	NeuroMab	75-407	1:200	RRID:AB_2877588

Synapse quantification

Synaptic density quantification was performed in Fiji. tdTomato fluorescence was used to visualize the neurites and determine the neurite area, while Syn1 fluorescence was used visualize synaptic puncta. Puncta number and area were quantified using Fiji particle analyzer. To quantify hRGCs axonal Syn1 levels in microfluidic devices, a color threshold of merged tdTomato and Syn1 images was set before using the particle analyzer. This step enabled quantification of Syn1 levels specifically in hRGC axons and excluded Syn1 in LGN, SCN, or OFB neurons.

Neurite reconstruction

hRGCs in 12mm coverslips were transfected by Lipofectamine 3000 (Life technologies, cat# L3000001) with 500 µg of pAAV-hSyn1-EGFP-P2A-EGFPf-WPRE-HGHpA plasmid (Addgene, cat# 74513) following manual instructions. Fresh medium was replaced after 6 hours of transfection to prevent cell toxicity. hRGCs were fixed after 48 hours of transfection following immunocytochemistry with GFP antibody staining. The tile images were acquired using ZEISS Axio Observer and processed in Fiji using a neuroanatomy plug-in for neurite tracing and Sholl analysis.

Statistical analysis

All experimental data are presented as mean ± s.e.m., with n indicating the number of replicates across all experiments. Statistical analyses were performed using either Student's t-test or ANOVA followed by Tukey's post hoc test, utilizing GraphPad Prism 10. Statistical significance was defined as $p < 0.05$ for all experiments.

Acknowledgments

We thank Dr. Matthew N. Rasband for kindly sharing antibodies, and Dr. Peter Bor-Chan Lin for assisting in the establishment of LGN and SCN mouse dissection techniques. We thank the Optical Imaging and Vital Microscopy Core at Baylor College of Medicine for technical support. This work was supported by the National Institutes of Health (NIH, grants R01EY033772, R01EY035254, R01EY032566, R01EY030458, and R21AG074163 to M.A.S. and R01EY033022 and U24EY033269 to J.S.M.) and the Foundation Fighting

Blindness (to M.A.S.). This work was also supported by the RReSTORE Consortium (to K.H).

References

1. Martersteck, E.M., Hirokawa, K.E., Evarts, M., Bernard, A., Duan, X., Li, Y., Ng, L., Oh, S.W., Ouellette, B., Royall, J.J., et al. (2017). Diverse Central Projection Patterns of Retinal Ganglion Cells. Cell Rep *18*, 2058-2072. 10.1016/j.celrep.2017.01.075.
2. Dhande, O.S., Stafford, B.K., Lim, J.A., and Huberman, A.D. (2015). Contributions of Retinal Ganglion Cells to Subcortical Visual Processing and Behaviors. Annu Rev Vis Sci *1*, 291-328. 10.1146/annurev-vision-082114-035502.
3. Huang, K.C., Tawfik, M., and Samuel, M.A. (2024). Retinal ganglion cell circuits and glial interactions in humans and mice. Trends Neurosci *47*, 994-1013. 10.1016/j.tins.2024.09.010.
4. Villegas-Perez, M.P., Vidal-Sanz, M., Bray, G.M., and Aguayo, A.J. (1988). Influences of peripheral nerve grafts on the survival and regrowth of axotomized retinal ganglion cells in adult rats. J Neurosci *8*, 265-280. 10.1523/JNEUROSCI.08-01-00265.1988.
5. Park, K.K., Liu, K., Hu, Y., Smith, P.D., Wang, C., Cai, B., Xu, B., Connolly, L., Kramvis, I., Sahin, M., and He, Z. (2008). Promoting axon regeneration in the adult CNS by modulation of the PTEN/mTOR pathway. Science *322*, 963-966. 10.1126/science.1161566.
6. Syc-Mazurek, S.B., and Libby, R.T. (2019). Axon injury signaling and compartmentalized injury response in glaucoma. Prog Retin Eye Res *73*, 100769. 10.1016/j.preteyeres.2019.07.002.
7. Whitmore, A.V., Libby, R.T., and John, S.W. (2005). Glaucoma: thinking in new ways-a role for autonomous axonal self-destruction and other compartmentalised processes? Prog Retin Eye Res *24*, 639-662. 10.1016/j.preteyeres.2005.04.004.
8. Goetz, J., Jessen, Z.F., Jacobi, A., Mani, A., Cooler, S., Greer, D., Kadri, S., Segal, J., Shekhar, K., Sanes, J.R., and Schwartz, G.W. (2022). Unified classification of mouse retinal ganglion cells using function, morphology, and gene expression. Cell Rep *40*, 111040. 10.1016/j.celrep.2022.111040.
9. Li, J., Choi, J., Cheng, X., Ma, J., Pema, S., Sanes, J.R., Mardon, G., Frankfort, B.J., Tran, N.M., Li, Y., and Chen, R. (2024). Comprehensive single-cell atlas of the mouse retina. iScience *27*, 109916. 10.1016/j.isci.2024.109916.

10. Masri, R.A., Percival, K.A., Koizumi, A., Martin, P.R., and Grunert, U. (2019). Survey of retinal ganglion cell morphology in marmoset. J Comp Neurol *527*, 236-258. 10.1002/cne.24157.
11. Zhang, L., Cavallini, M., Wang, J., Xin, R., Zhang, Q., Feng, G., Sanes, J.R., and Peng, Y.R. (2024). Evolutionary and developmental specialization of foveal cell types in the marmoset. Proc Natl Acad Sci U S A *121*, e2313820121. 10.1073/pnas.2313820121.
12. Grunert, U., and Martin, P.R. (2020). Cell types and cell circuits in human and non-human primate retina. Prog Retin Eye Res, 100844. 10.1016/j.preteyeres.2020.100844.
13. Hahn, J., Monavarfeshani, A., Qiao, M., Kao, A.H., Kolsch, Y., Kumar, A., Kunze, V.P., Rasys, A.M., Richardson, R., Wekselblatt, J.B., et al. (2023). Evolution of neuronal cell classes and types in the vertebrate retina. Nature *624*, 415-424. 10.1038/s41586-023-06638-9.
14. Grunert, U., and Martin, P.R. (2021). Morphology, Molecular Characterization, and Connections of Ganglion Cells in Primate Retina. Annu Rev Vis Sci *7*, 73-103. 10.1146/annurev-vision-100419-115801.
15. Cowan, C.S., Renner, M., De Gennaro, M., Gross-Scherf, B., Goldblum, D., Hou, Y., Munz, M., Rodrigues, T.M., Krol, J., Szikra, T., et al. (2020). Cell Types of the Human Retina and Its Organoids at Single-Cell Resolution. Cell *182*, 1623-1640 e1634. 10.1016/j.cell.2020.08.013.
16. Fligor, C.M., Lavekar, S.S., Harkin, J., Shields, P.K., VanderWall, K.B., Huang, K.C., Gomes, C., and Meyer, J.S. (2021). Extension of retinofugal projections in an assembled model of human pluripotent stem cell-derived organoids. Stem Cell Reports *16*, 2228-2241. 10.1016/j.stemcr.2021.05.009.
17. Perry, V.H., and Cowey, A. (1984). Retinal ganglion cells that project to the superior colliculus and pretectum in the macaque monkey. Neuroscience *12*, 1125-1137. 10.1016/0306-4522(84)90007-1.
18. Do, M.T., and Yau, K.W. (2010). Intrinsically photosensitive retinal ganglion cells. Physiol Rev *90*, 1547-1581. 10.1152/physrev.00013.2010.
19. Sluch, V.M., Chamling, X., Liu, M.M., Berlinicke, C.A., Cheng, J., Mitchell, K.L., Welsbie, D.S., and Zack, D.J. (2017). Enhanced Stem Cell Differentiation and Immunopurification of Genome Engineered Human Retinal Ganglion Cells. Stem Cells Transl Med *6*, 1972-1986. 10.1002/sctm.17-0059.
20. Marquardt, T., and Gruss, P. (2002). Generating neuronal diversity in the retina: one for nearly all. Trends Neurosci *25*, 32-38. 10.1016/s0166-2236(00)02028-2.
21. Nguyen-Ba-Charvet, K.T., and Rebsam, A. (2020). Neurogenesis and Specification of Retinal Ganglion Cells. Int J Mol Sci *21*. 10.3390/ijms21020451.
22. Fligor, C.M., Langer, K.B., Sridhar, A., Ren, Y., Shields, P.K., Edler, M.C., Ohlemacher, S.K., Sluch, V.M., Zack, D.J., Zhang, C., et al. (2018). Three-

Dimensional Retinal Organoids Facilitate the Investigation of Retinal Ganglion Cell Development, Organization and Neurite Outgrowth from Human Pluripotent Stem Cells. Sci Rep *8*, 14520. 10.1038/s41598-018-32871-8.
23. Capowski, E.E., Samimi, K., Mayerl, S.J., Phillips, M.J., Pinilla, I., Howden, S.E., Saha, J., Jansen, A.D., Edwards, K.L., Jager, L.D., et al. (2019). Reproducibility and staging of 3D human retinal organoids across multiple pluripotent stem cell lines. Development *146*. 10.1242/dev.171686.
24. Lu, Y., Shiau, F., Yi, W., Lu, S., Wu, Q., Pearson, J.D., Kallman, A., Zhong, S., Hoang, T., Zuo, Z., et al. (2020). Single-Cell Analysis of Human Retina Identifies Evolutionarily Conserved and Species-Specific Mechanisms Controlling Development. Dev Cell *53*, 473-491 e479. 10.1016/j.devcel.2020.04.009.
25. Bernhardt, R., and Matus, A. (1982). Initial phase of dendrite growth: evidence for the involvement of high molecular weight microtubule-associated proteins (HMWP) before the appearance of tubulin. J Cell Biol *92*, 589-593. 10.1083/jcb.92.2.589.
26. Kordeli, E., Lambert, S., and Bennett, V. (1995). AnkyrinG. A new ankyrin gene with neural-specific isoforms localized at the axonal initial segment and node of Ranvier. J Biol Chem *270*, 2352-2359. 10.1074/jbc.270.5.2352.
27. Anton-Fernandez, A., Leon-Espinosa, G., DeFelipe, J., and Munoz, A. (2022). Pyramidal cell axon initial segment in Alzheimer s disease. Sci Rep *12*, 8722. 10.1038/s41598-022-12700-9.
28. Sohn, P.D., Huang, C.T., Yan, R., Fan, L., Tracy, T.E., Camargo, C.M., Montgomery, K.M., Arhar, T., Mok, S.A., Freilich, R., et al. (2019). Pathogenic Tau Impairs Axon Initial Segment Plasticity and Excitability Homeostasis. Neuron *104*, 458-470 e455. 10.1016/j.neuron.2019.08.008.
29. Escobedo, G., Jr., Wu, Y., Ogawa, Y., Ding, X., and Rasband, M.N. (2024). An evolutionarily conserved AnkyrinG-dependent motif clusters axonal K2P K+ channels. J Cell Biol *223*. 10.1083/jcb.202401140.
30. Kiral, F.R., Cakir, B., Tanaka, Y., Kim, J., Yang, W.S., Wehbe, F., Kang, Y.J., Zhong, M., Sancer, G., Lee, S.H., et al. (2023). Generation of ventralized human thalamic organoids with thalamic reticular nucleus. Cell Stem Cell *30*, 677-688 e675. 10.1016/j.stem.2023.03.007.
31. Kim, J.I., Miura, Y., Li, M.Y., Revah, O., Selvaraj, S., Birey, F., Meng, X., Thete, M.V., Pavlov, S.D., Andersen, J., et al. (2024). Human assembloids reveal the consequences of CACNA1G gene variants in the thalamocortical pathway. Neuron *112*, 4048-4059 e4047. 10.1016/j.neuron.2024.09.020.
32. Suzuki-Hirano, A., Ogawa, M., Kataoka, A., Yoshida, A.C., Itoh, D., Ueno, M., Blackshaw, S., and Shimogori, T. (2011). Dynamic spatiotemporal gene expression in embryonic mouse thalamus. J Comp Neurol *519*, 528-543. 10.1002/cne.22531.
33. Mashiko, H., Yoshida, A.C., Kikuchi, S.S., Niimi, K., Takahashi, E., Aruga, J., Okano, H., and Shimogori, T. (2012). Comparative anatomy of marmoset and

mouse cortex from genomic expression. J Neurosci *32*, 5039-5053. 10.1523/JNEUROSCI.4788-11.2012.
34. Aton, S.J., Colwell, C.S., Harmar, A.J., Waschek, J., and Herzog, E.D. (2005). Vasoactive intestinal polypeptide mediates circadian rhythmicity and synchrony in mammalian clock neurons. Nat Neurosci *8*, 476-483. 10.1038/nn1419.
35. Abrahamson, E.E., and Moore, R.Y. (2001). Suprachiasmatic nucleus in the mouse: retinal innervation, intrinsic organization and efferent projections. Brain Res *916*, 172-191. 10.1016/s0006-8993(01)02890-6.
36. Tervo, D.G., Hwang, B.Y., Viswanathan, S., Gaj, T., Lavzin, M., Ritola, K.D., Lindo, S., Michael, S., Kuleshova, E., Ojala, D., et al. (2016). A Designer AAV Variant Permits Efficient Retrograde Access to Projection Neurons. Neuron *92*, 372-382. 10.1016/j.neuron.2016.09.021.
37. von Bartheld, C.S., Byers, M.R., Williams, R., and Bothwell, M. (1996). Anterograde transport of neurotrophins and axodendritic transfer in the developing visual system. Nature *379*, 830-833. 10.1038/379830a0.
38. Fernando, M., Lee, S., Wark, J.R., Xiao, D., Lim, B.Y., O'Hara-Wright, M., Kim, H.J., Smith, G.C., Wong, T., Teber, E.T., et al. (2022). Differentiation of brain and retinal organoids from confluent cultures of pluripotent stem cells connected by nerve-like axonal projections of optic origin. Stem Cell Reports *17*, 1476-1492. 10.1016/j.stemcr.2022.04.003.
39. Gabriel, E., Albanna, W., Pasquini, G., Ramani, A., Josipovic, N., Mariappan, A., Riparbelli, M.G., Callaini, G., Karch, C.M., Goureau, O., et al. (2023). Generation of iPSC-derived human forebrain organoids assembling bilateral eye primordia. Nat Protoc *18*, 1893-1929. 10.1038/s41596-023-00814-x.
40. Liu, W., Shrestha, R., Lowe, A., Zhang, X., and Spaeth, L. (2023). Self-formation of concentric zones of telencephalic and ocular tissues and directional retinal ganglion cell axons. Elife *12*. 10.7554/eLife.87306.
41. Mason, C., and Slavi, N. (2020). Retinal Ganglion Cell Axon Wiring Establishing the Binocular Circuit. Annu Rev Vis Sci *6*, 215-236. 10.1146/annurev-vision-091517-034306.
42. Delpech, C., Schaeffer, J., Vilallongue, N., Delaunay, A., Benadjal, A., Blot, B., Excoffier, B., Plissonnier, E., Gascon, E., Albert, F., et al. (2024). Axon guidance during mouse central nervous system regeneration is required for specific brain innervation. Dev Cell *59*, 3213-3228 e3218. 10.1016/j.devcel.2024.09.005.
43. Ma, Y.T., Hsieh, T., Forbes, M.E., Johnson, J.E., and Frost, D.O. (1998). BDNF injected into the superior colliculus reduces developmental retinal ganglion cell death. J Neurosci *18*, 2097-2107. 10.1523/JNEUROSCI.18-06-02097.1998.
44. Isenmann, S., Klocker, N., Gravel, C., and Bahr, M. (1998). Short communication: protection of axotomized retinal ganglion cells by

adenovirally delivered BDNF in vivo. Eur J Neurosci *10*, 2751-2756. 10.1046/j.1460-9568.1998.00325.x.
45. Lom, B., and Cohen-Cory, S. (1999). Brain-derived neurotrophic factor differentially regulates retinal ganglion cell dendritic and axonal arborization in vivo. J Neurosci *19*, 9928-9938. 10.1523/JNEUROSCI.19-22-09928.1999.
46. Pease, M.E., McKinnon, S.J., Quigley, H.A., Kerrigan-Baumrind, L.A., and Zack, D.J. (2000). Obstructed axonal transport of BDNF and its receptor TrkB in experimental glaucoma. Invest Ophthalmol Vis Sci *41*, 764-774.
47. Claes, M., Geeraerts, E., Plaisance, S., Mentens, S., Van den Haute, C., De Groef, L., Arckens, L., and Moons, L. (2022). Chronic Chemogenetic Activation of the Superior Colliculus in Glaucomatous Mice: Local and Retrograde Molecular Signature. Cells *11*. 10.3390/cells11111784.
48. Su, J., Charalambakis, N.E., Sabbagh, U., Somaiya, R.D., Monavarfeshani, A., Guido, W., and Fox, M.A. (2020). Retinal inputs signal astrocytes to recruit interneurons into visual thalamus. Proc Natl Acad Sci U S A *117*, 2671-2682. 10.1073/pnas.1913053117.
49. Huang, K.C., Gomes, C., Shiga, Y., Belforte, N., VanderWall, K.B., Lavekar, S.S., Fligor, C.M., Harkin, J., Hetzer, S.M., Patil, S.V., et al. (2024). Acquisition of neurodegenerative features in isogenic OPTN(E50K) human stem cell-derived retinal ganglion cells associated with autophagy disruption and mTORC1 signaling reduction. Acta Neuropathol Commun *12*, 164. 10.1186/s40478-024-01872-2.
50. VanderWall, K.B., Huang, K.C., Pan, Y., Lavekar, S.S., Fligor, C.M., Allsop, A.R., Lentsch, K.A., Dang, P., Zhang, C., Tseng, H.C., et al. (2020). Retinal Ganglion Cells With a Glaucoma OPTN(E50K) Mutation Exhibit Neurodegenerative Phenotypes when Derived from Three-Dimensional Retinal Organoids. Stem Cell Reports *15*, 52-66. 10.1016/j.stemcr.2020.05.009.
51. Rezaie, T., Child, A., Hitchings, R., Brice, G., Miller, L., Coca-Prados, M., Heon, E., Krupin, T., Ritch, R., Kreutzer, D., et al. (2002). Adult-onset primary open-angle glaucoma caused by mutations in optineurin. Science *295*, 1077-1079. 10.1126/science.1066901.
52. Rozpedek-Kaminska, W., Wojtczak, R., Szaflik, J.P., Szaflik, J., and Majsterek, I. (2020). The Genetic and Endoplasmic Reticulum-Mediated Molecular Mechanisms of Primary Open-Angle Glaucoma. Int J Mol Sci *21*. 10.3390/ijms21114171.
53. Skowronska-Krawczyk, D., Zhao, L., Zhu, J., Weinreb, R.N., Cao, G., Luo, J., Flagg, K., Patel, S., Wen, C., Krupa, M., et al. (2015). P16INK4a Upregulation Mediated by SIX6 Defines Retinal Ganglion Cell Pathogenesis in Glaucoma. Mol Cell *59*, 931-940. 10.1016/j.molcel.2015.07.027.
54. Shiga, Y., Akiyama, M., Nishiguchi, K.M., Sato, K., Shimozawa, N., Takahashi, A., Momozawa, Y., Hirata, M., Matsuda, K., Yamaji, T., et al. (2018). Genome-

wide association study identifies seven novel susceptibility loci for primary open-angle glaucoma. Hum Mol Genet *27*, 1486-1496. 10.1093/hmg/ddy053.
55. Tseng, H.C., Riday, T.T., McKee, C., Braine, C.E., Bomze, H., Barak, I., Marean-Reardon, C., John, S.W., Philpot, B.D., and Ehlers, M.D. (2015). Visual impairment in an optineurin mouse model of primary open-angle glaucoma. Neurobiol Aging *36*, 2201-2212. 10.1016/j.neurobiolaging.2015.02.012.
56. Aung, T., Rezaie, T., Okada, K., Viswanathan, A.C., Child, A.H., Brice, G., Bhattacharya, S.S., Lehmann, O.J., Sarfarazi, M., and Hitchings, R.A. (2005). Clinical features and course of patients with glaucoma with the E50K mutation in the optineurin gene. Invest Ophthalmol Vis Sci *46*, 2816-2822. 10.1167/iovs.04-1133.
57. Quigley, H.A., Addicks, E.M., Green, W.R., and Maumenee, A.E. (1981). Optic nerve damage in human glaucoma. II. The site of injury and susceptibility to damage. Arch Ophthalmol *99*, 635-649. 10.1001/archopht.1981.03930010635009.
58. Perry, V.H., Oehler, R., and Cowey, A. (1984). Retinal ganglion cells that project to the dorsal lateral geniculate nucleus in the macaque monkey. Neuroscience *12*, 1101-1123. 10.1016/0306-4522(84)90006-x.
59. Fligor, C.M., Huang, K.C., Lavekar, S.S., VanderWall, K.B., and Meyer, J.S. (2020). Differentiation of retinal organoids from human pluripotent stem cells. Methods Cell Biol *159*, 279-302. 10.1016/bs.mcb.2020.02.005.
60. Ohlemacher, S.K., Iglesias, C.L., Sridhar, A., Gamm, D.M., and Meyer, J.S. (2015). Generation of highly enriched populations of optic vesicle-like retinal cells from human pluripotent stem cells. Curr Protoc Stem Cell Biol *32*, 1H 8 1-1H 8 20. 10.1002/9780470151808.sc01h08s32.
61. Meyer, J.S., Shearer, R.L., Capowski, E.E., Wright, L.S., Wallace, K.A., McMillan, E.L., Zhang, S.C., and Gamm, D.M. (2009). Modeling early retinal development with human embryonic and induced pluripotent stem cells. Proc Natl Acad Sci U S A *106*, 16698-16703. 10.1073/pnas.0905245106.

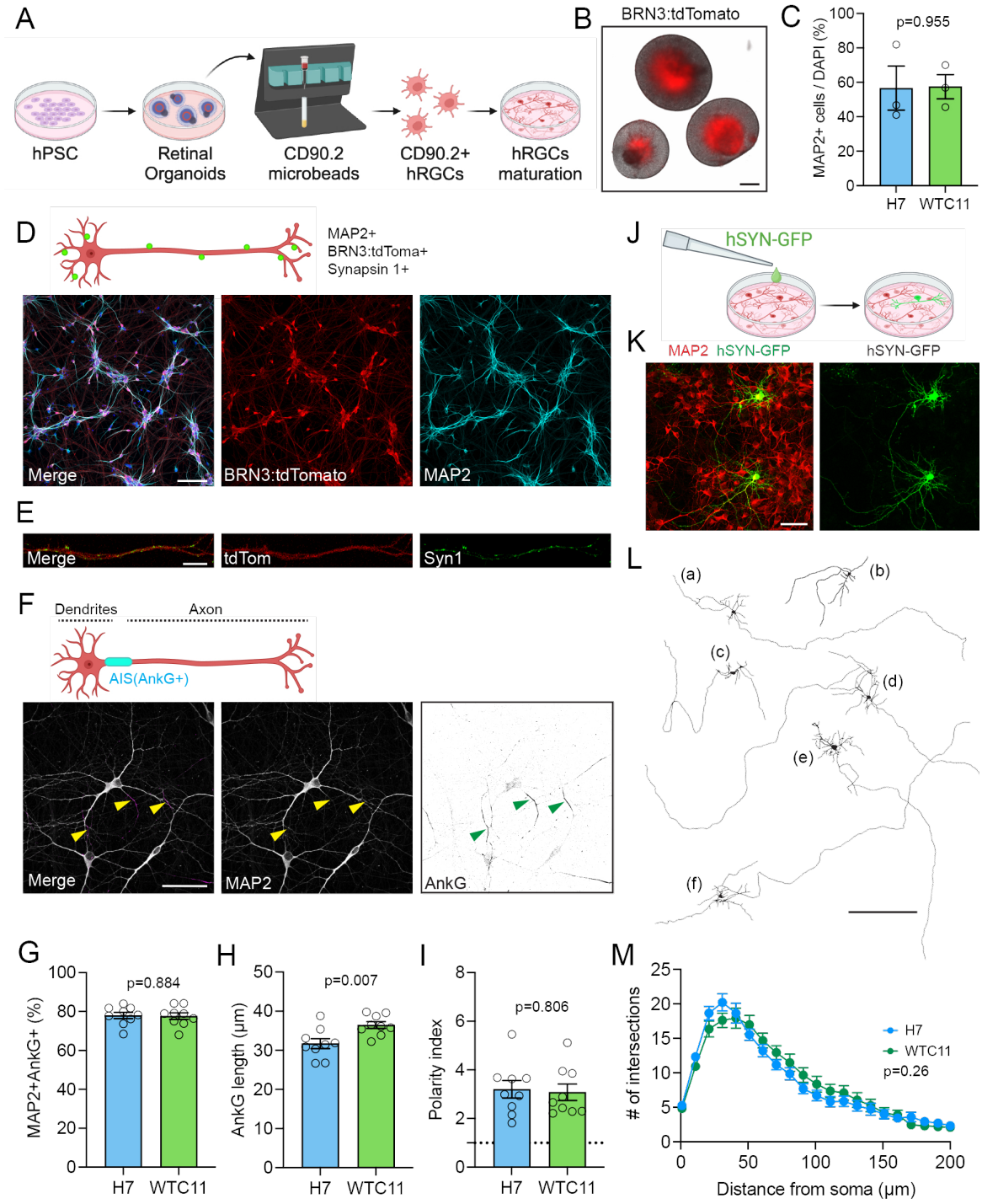

Figure 1: hRGCs mature and polarize in long term cultures. A. Schematic of hRGC generation and isolation using CD90 (Thy1.2) conjugated magnetic beads. This approach

can be used to purify hRGCs from both hESC line H7, which carries tdTomato-Thy1.2, and the iPSC line WTC11, which carries Thy1.2 alone under the transcription factor BRN3. **B**. hRGCs can be identified in the inner retinal layers of organoids generated from the H7 tdTomato-Thy1.2 line. Scale bar = 200 μm. **C.** Quantification of hRGC purity from both the WTC11 and the H7 iPSC lines. n = 3 biological replicates cultures and >200 cells were count per biological replicates from both lines. **D**. Representative images of hRGCs at three weeks post plating. hRGCs (tdTomato, red) express high levels of the dendrite marker MAP2 (cyan) clustered around the cell somas. Scale bar = 100μm. **E**. Representative images of hRGCs following staining for the synapse marker Syn 1 (green) at three weeks post plating. Scale bar = 10μm. **F**. Representative images of hRGCs following staining for the dendrite marker MAP2 (grey) and the axon initial segment marker Ankyrin G (AnkG, magenta). At three weeks post plating, hRGCs show distinct axon initial segments (AISs), which appear close the soma (arrows). Scale bars = 100μm. **G.** Quantification of hRGCs derived from both hPSC lines show that the majority of cells possess an AIS. There is no significant difference the number of neurons with an AIS between the two lines. **H**. Quantification of AIS length in hRGCs following staining with AnkG. In both cell lines, the AIS is 30-40μm long, with those in WTC11 derived hRGCs appearing slightly longer. **I**. The polarity index was calculated as the intensity ratio of MAP2 and AnkG. Both cell lines exhibited strong polarization, with polarity index values ranging from 2 to 4, and no significant differences were observed between the hRGC groups (n = 9 images from 3 biological replications, each image contains >20 hRGCs). **J**. Schematic of sparse labeling hRGCs using lipofectamine transfection. **K.** Representative images of hRGCs a week after hSYN-GFP sparse labeling. Scale bar = 50μm **L.** Representative images of single hRGC neurite reconstruction. Scale bar = 1000μm. **M**.

Sholl analysis revealed that most hRGCs displayed a high density of neurites near the soma, consistent with dendrite and axon segregation. No significant differences were detected between hRGCs derived from the two hPSC lines. n = 18-19 hRGCs from 3 biological replicates in both hPSC lines. Data are presented as average values ± the s.e.m.

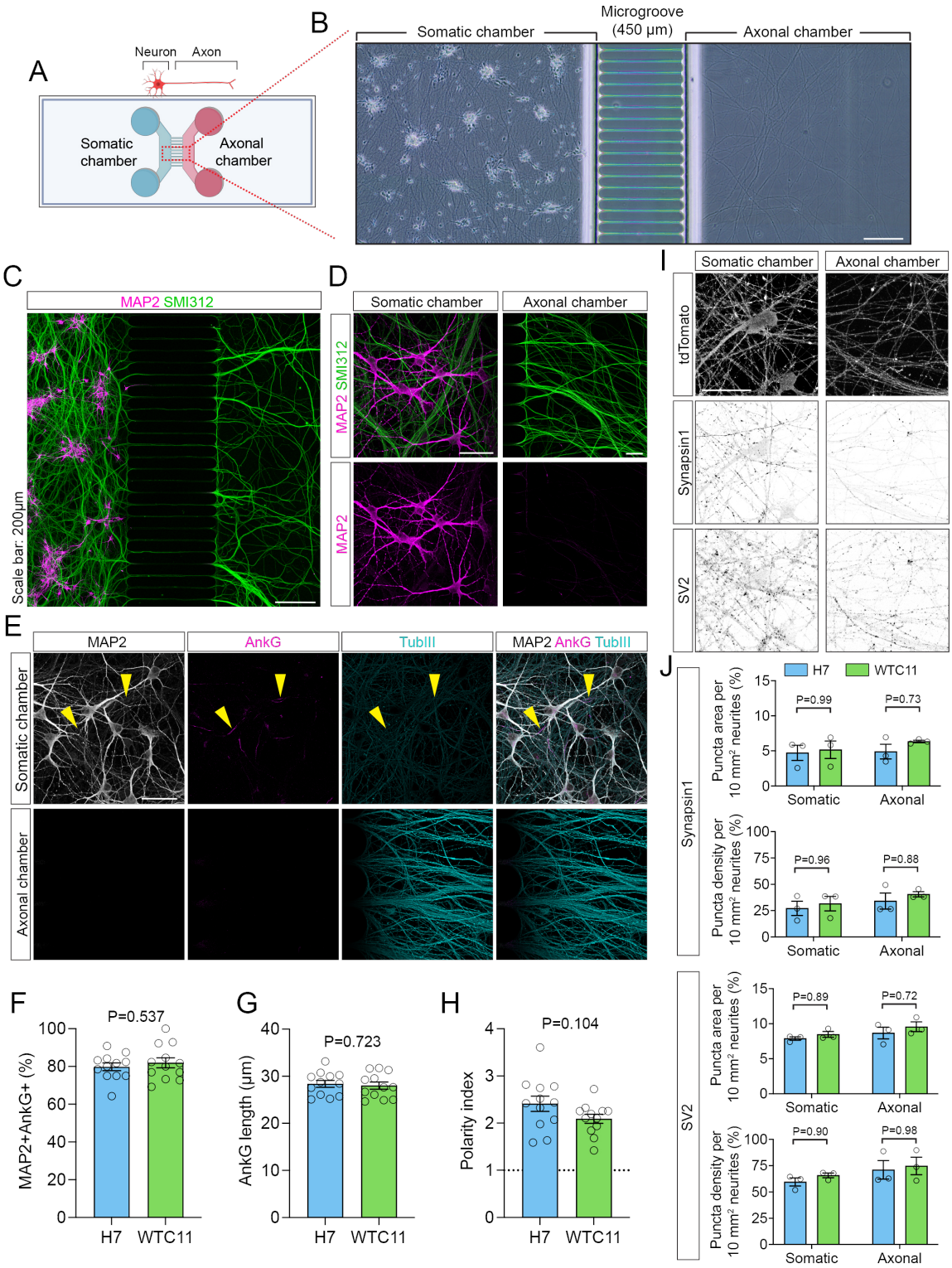

Figure 2. hRGCs show proper polarization in a microfluidics system. A-B. Schematic (**A**) and representative bright field images (**B**) of the organization of the

microfluidics system. hRGCs are plated in the somatic chamber and extend axons through 450 um microgroove to the axonal chamber. Scale bars = 200μm. **C-D**. Representative low magnification (**C**) and high magnification (**D**) images of hRGCs grown in the microfluidics system with the dendritic marker MAP2 and the axonal marker SMI312 labeling. Scale bars = 50μm. **E.** Representative images of axon maturation show that hRGCs develop defined axon initial segments that are proximal to the cell body, localized to axons [TubIII positive (cyan) while MAP2 negative (greyscale)] and positive for structural protein AnkG (magenta, arrows). Scale bars = 50μm. **F-G**. Quantification of hRGCs in microfluidics chambers derived from both hPSC lines show that most cells possess an AIS (**F**) and that the length of the AIS is approximately ~30um. There is no significant difference in these values between hRGCs derived from the two H7 and WTC11 hPSC lines. **H.** The polarity index was calculated as the intensity ratio of MAP2 and AnkG. Both cell lines exhibited strong polarization, with polarity index values ranging from ~1,5 to 3.5, and no significant differences were observed between the hRGC groups (n = 12 images from 3 biological replications, each image contains >10 hRGCs). **I-J**. Representative images (**I**) and quantification (**J**) of the distribution, puncta area and puncta density of the synapse vesicle protein SV2 and synapse protein SYN1 in the somatic versus the axonal chamber of hRGCs cultured in the microfluidics system. Scale bars = 50μm. No significant differences were observed between the two lines or in the two compartments, though the density of SV2 positive puncta tended to be higher than that of SYN1 (n = 3 biological replications, each replicate was quantified from 4 images). Data are presented as average values ± the s.e.m.

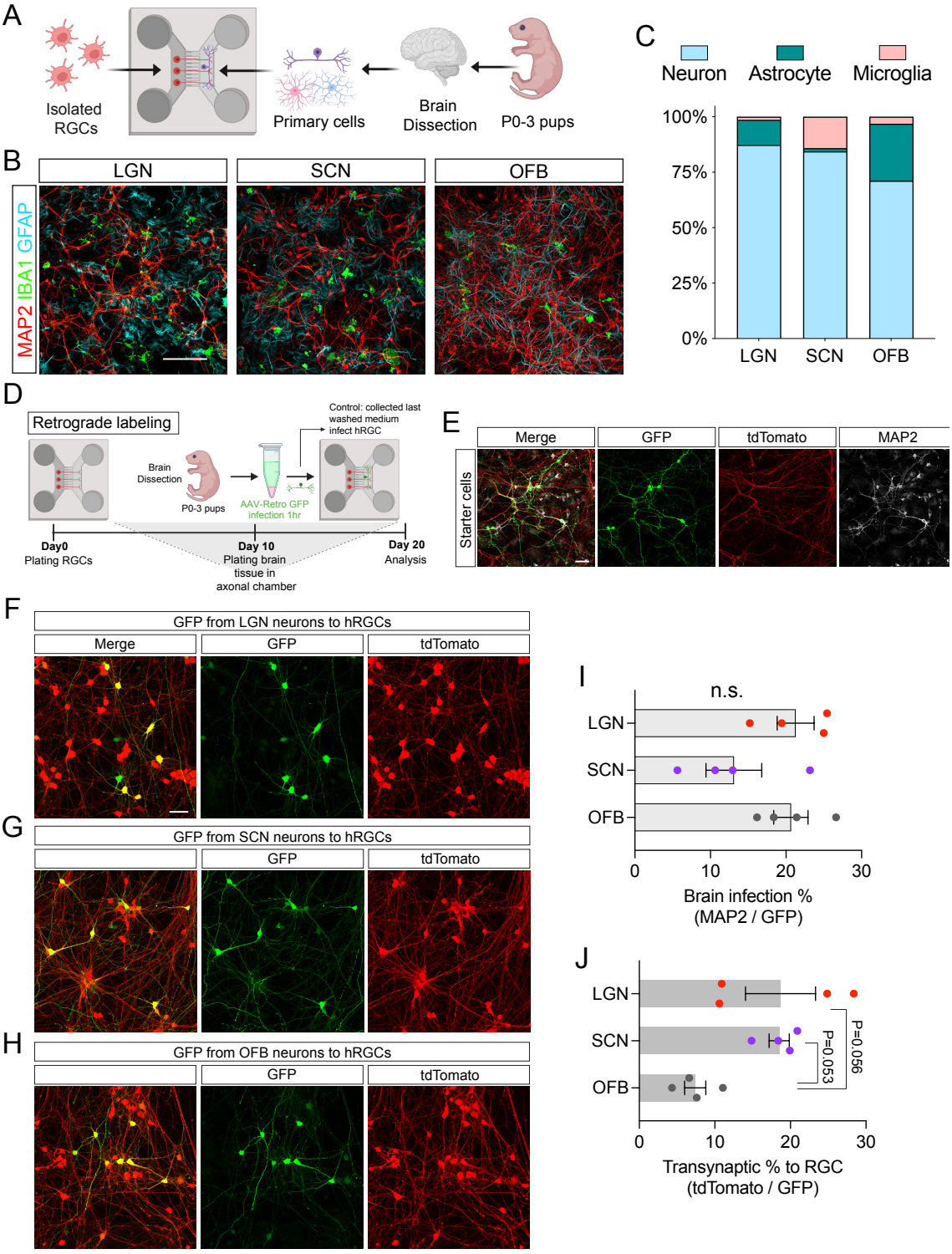
A
Isolated RGCs
Primary cells
Brain Dissection
P0-3 pups
B
LGN
SCN
OFB
MAP2 IBA1 GFAP
C
Neuron
Astrocyte
Microglia
100%
75%
50%
25%
0%
LGN
SCN
OFB
D
Retrograde labeling
Brain Dissection
P0-3 pups
AAV-Retro GFP infection 1hr
Control: collected last washed medium infect hRGC
Day0 Plating RGCs
Day 10 Plating brain tissue in axonal chamber
Day 20 Analysis
E
Merge
GFP
tdTomato
MAP2
Starter cells
F
GFP from LGN neurons to hRGCs
Merge
GFP
tdTomato
G
GFP from SCN neurons to hRGCs
GFP
tdTomato
H
GFP from OFB neurons to hRGCs
GFP
tdTomato
I
n.s.
LGN
SCN
OFB
0
10
20
30
Brain infection % (MAP2 / GFP)
J
LGN
SCN
OFB
P=0.056
P=0.053
0
10
20
30
Transynaptic % to RGC (tdTomato / GFP)

Figure 3. hRGCs form brain region specific connections with post-synaptic targets. **A**. Schematic of the generation and addition of retinorecipient and control brain regions to the microfluidics system. **B-C**. Representative images (**B**) and quantification of (**C**) of major cell type representation in the retinorecipient and control brain regions. Cultures from each region [lateral geniculate nucleus (LGN), superchiasmatic nucleus (SCN) and olfactory bulb (OFB)] were comprised primarily of neurons (MAP2, red, ~75-85%), while microglia (Iba, green), and astrocytes (GFAP, cyan) were also present. n = 8 images from 3 biological replicates. Scale bars = 50 µm **D**. Schematic of retrograde circuit tracing approach. hRGCs were grown in microfluidics chambers for 10 days. Following this period, dissociated cells from dissected control brain regions (OFB) and retinorecipient brain regions (LGN and SCN) were isolated from postnatal day (P) 0 to P3 mouse pups, infected with AAV-Retro GFP, washed extensively, and then plated in then plated in the axonal chamber. GFP positive cells were quantified in the somatic chamber 10 days later. **E.** Representative images of AAV infection in the starter brain cell populations. Scale bars = 50 µm. **F-H.** Representative images of the number of transsynaptic labeled, GFP positive hRGCs (tdTomato+) following retrograde tracing from retinorecipient LGN and SCN neurons or OFB control neurons. Scale bars = 50 µm. **I-J.** Quantification of AAV infection in the starter brain cells and transsynaptically labeled in hRGCs. No significant difference in AAV-Retro-GFP (green) was observed between the starter cell populations **(I)**. While a degree of connectivity was observed in all cases, LGN and SCN neurons tended to have higher degrees of connectivity relative to control OFB neurons (**J**). n = 4 tile images from 2 biological replicates, each image contains >200 neurons or hRGCs. Data are presented as averaged average values from 3 to 4 independent experiments ± the s.e.m.

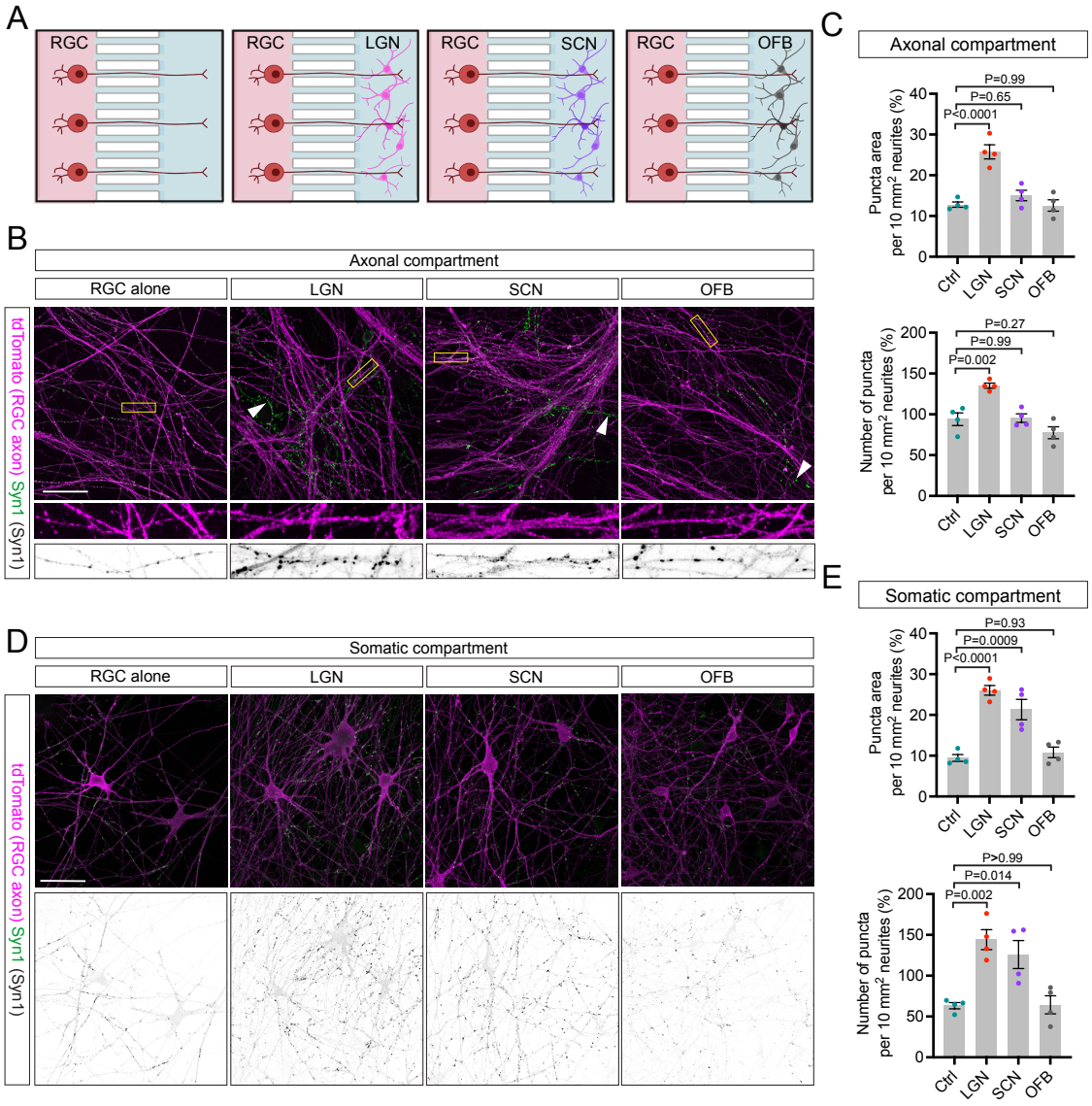

Figure 4: Retinorecipient targets specifically hRGC synapse formation. A. Schematic of the microfluidics system following the addition of diverse post-synaptic targets to the axonal chamber, lateral geniculate nucleus (LGN), superchiasmatic nucleus (SCN) and olfactory bulb (OFB). **B-C**. Representative images (**B**) and quantification (**C**) of Synapsin 1 (SYN1, green) along hRGC axons (tdTomato, magenta) following the

addition of dissociated cells from retinorecipient and control brain regions to the axonal chamber (white arrows). The addition of LGN partners significantly enhanced Syn1 puncta area and puncta number relative to hRGCs alone (Ctrl), SCN, or OFB partners (n = 4 biological replications, each replicate was quantified from 4 images). Scale bars = 50 µm. **D-E**. Representative images (**D**) and quantification (**D**) of Synapsin 1 (Syn1, GFP) along hRGC dendrites (tdTomato, magenta) in the somatic chamber following the addition of dissociated cells from retinorecipient and control brain regions to the axonal chamber. The addition of either retinorecipient partner (LGN, SCN) significantly enhanced hRGC maturation as indicated by the increase in Syn1 puncta area and puncta number relative to hRGCs alone (Ctrl) or OFB partners.n = 4 biological replicates, and 4 images were used to quantify each replicate. Scale bars = 50 µm. Data are presented as average values ± the s.e.m.

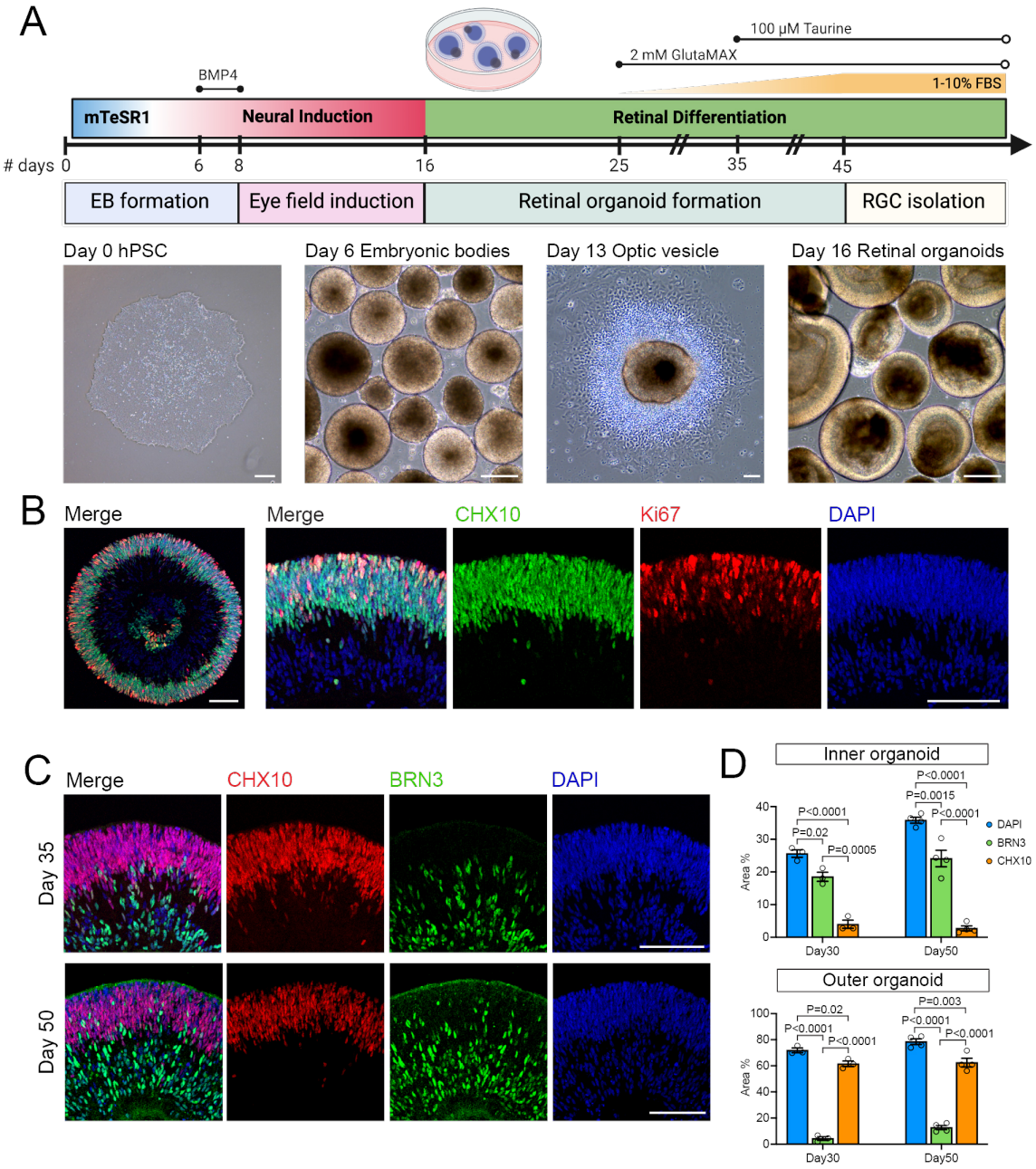

Supplemental Figure 1. Generation of hRGCs from hPSC-derived retinal organoids.

A. Schematic (upper panel) and representative images (lower panel) of the stages and the timeline for the induction of retinal organoids and RGC isolation. hRGCs were isolated from day 45 retina organoids for this study. Scale bars = 200μm. **B**. Cross section images

of a day 35 retinal organoid shows that the organoids have a spherical structure with properly layered developing retinal progenitor cells (CHX10, green) in the outer retina that are actively cycling (Ki67, red). Fate committed cells migrate to the inner retina and are negative for these markers but positive for then nuclear marker DAPI (blue). Scale bars = 100μm. **C-E**. Representative cross section images (**C**) and quantification (**D**) comparing day 35 and day 50 retinal organoids. Developing human retinal organoids conserve spatial and temporal developmental patterns observed in the developing human eye. At day 35, subsets of fate committed RGCs (BRN3, green) can be observed developing within the inner retina, while retina progenitor cells remain in the outer retina (CHX10, red, **D**). By day 50, increased numbers of RGCs are observed in the inner retina, and the numbers of retinal progenitor cells are decreased (CHX10, red, **E)** n = 3 to 4 biological replicates for both day 30 and 50 retinal organoids. Scale bar = 100 μm. Data are presented as average values ± the s.e.m.

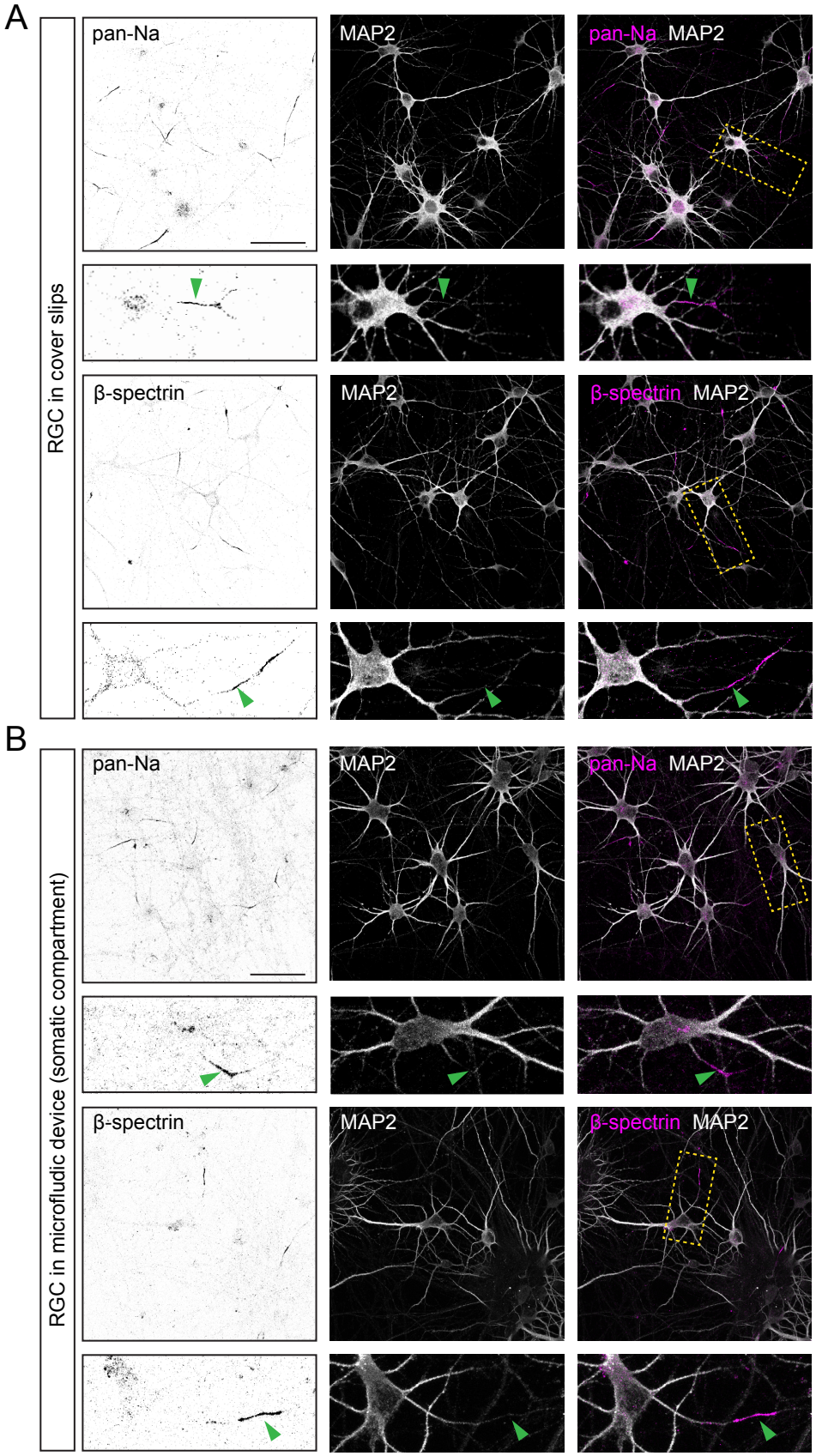
A
RGC in cover slips
pan-Na
MAP2
pan-Na MAP2
β-spectrin
MAP2
β-spectrin MAP2
B
RGC in microfludic device (somatic compartment)
pan-Na
MAP2
pan-Na MAP2
β-spectrin
MAP2
β-spectrin MAP2

Supplemental Figure 2: Differentiated hRGCs show additional axon initial segment localized proteins. A-B. Representative images from hRGCs in coverslips alone (**A**) or after culturing in microfluidics devices (**B**) for a period of 10 days following. Samples were stained for sodium channels (pan-Na, magenta upper panels) and β-Spectrin, both of which are known to be enriched in mature axon initial segments (AIS). In all cases, sodium channels and β-Spectrin were concentrated at AISs and were located proximal to the cell bodies of hRGCs (MAP2, white) both in coverslip conditions and in the microfluidics system (green arrows). Scale bars = 50 μm.

A

Neurons in LGN

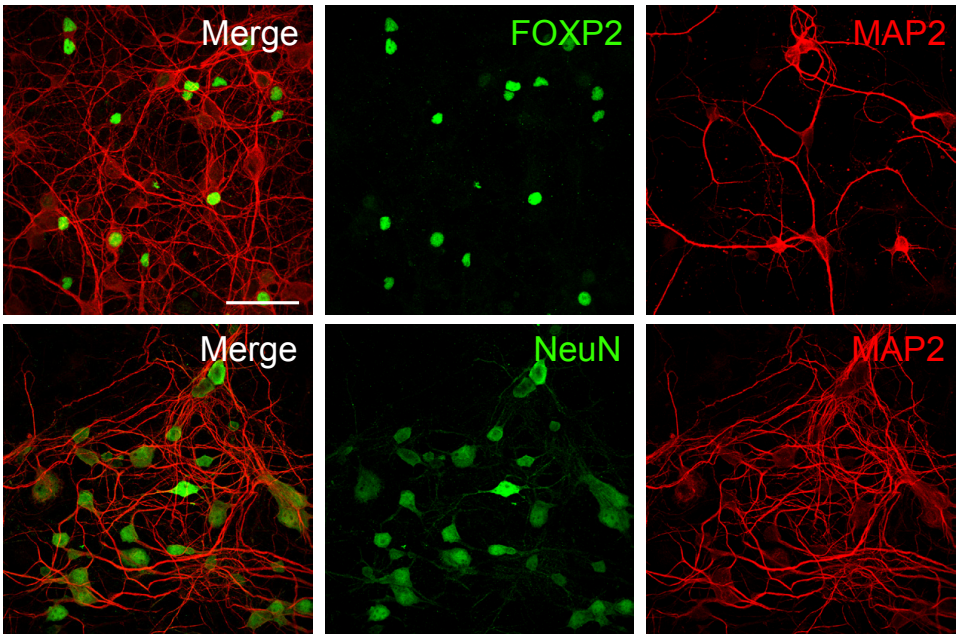

B

Neurons in SCN

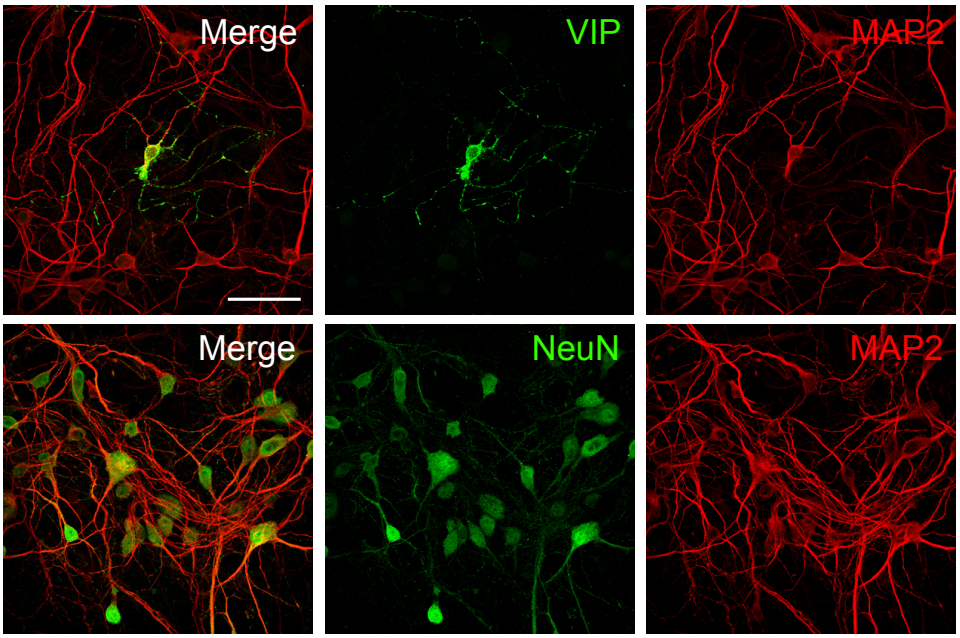

Supplemental Figure 3. Cultured retinorecipient neurons express region-specific markers. A. Representative images of neurons in lateral geniculate nucleus (LGN) cultures following staining for FOXP2, a transcription factor enriched in a subset of LGN neurons (green, upper panel) or the neuron marker NeuN (green, lower panel) together with staining for the dendritic marker MAP2. A subset of LGN neurons were positive for FOXP2, suggesting that appropriate neural identity is maintained in these cultures. **B**. Representative images of neurons in superchiasmatic nucleus (SCN) cultures following staining for vasoactive intestinal polypeptide (VIP), neurons essential for circadian entrainment (green, upper panel) or the neuron marker NeuN (green, lower panel) together with staining for the dendritic marker MAP2. Some SCN neurons were positive for VIP, suggesting that appropriate neural identity is also maintained in SCN cultures. Scale bars = 50 μm.

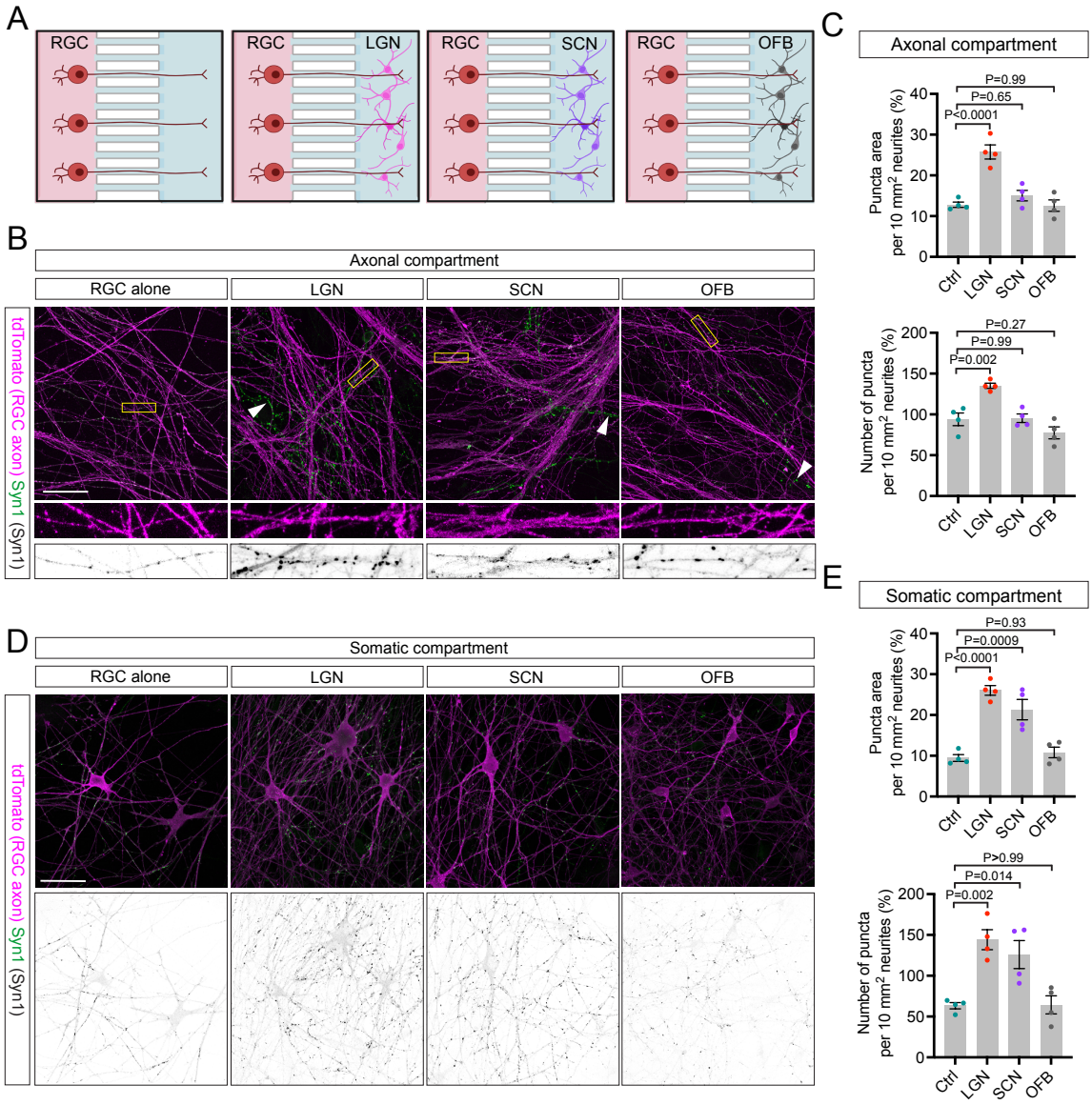

Supplemental Figure 4. hRGC axons colocalize with postsynaptic target neurites in the axonal chambers. A-C. Representative low and high magnification (crop) images of the dendrite marker MAP2 (green) and tdTomato positive hRGCs axons (magenta) following imaging of axonal chamber of the addition of lateral geniculate nucleus (LGN),

superchiasmatic nucleus (SCN), or olfactory bulb (OFB) post-synaptic targets. In each case, hRGC axons co-localized and interfaced with the dendrites of post-synaptic neurons, suggesting the potential for synapse formation (yellow arrows). Scale bars = 25 μm.

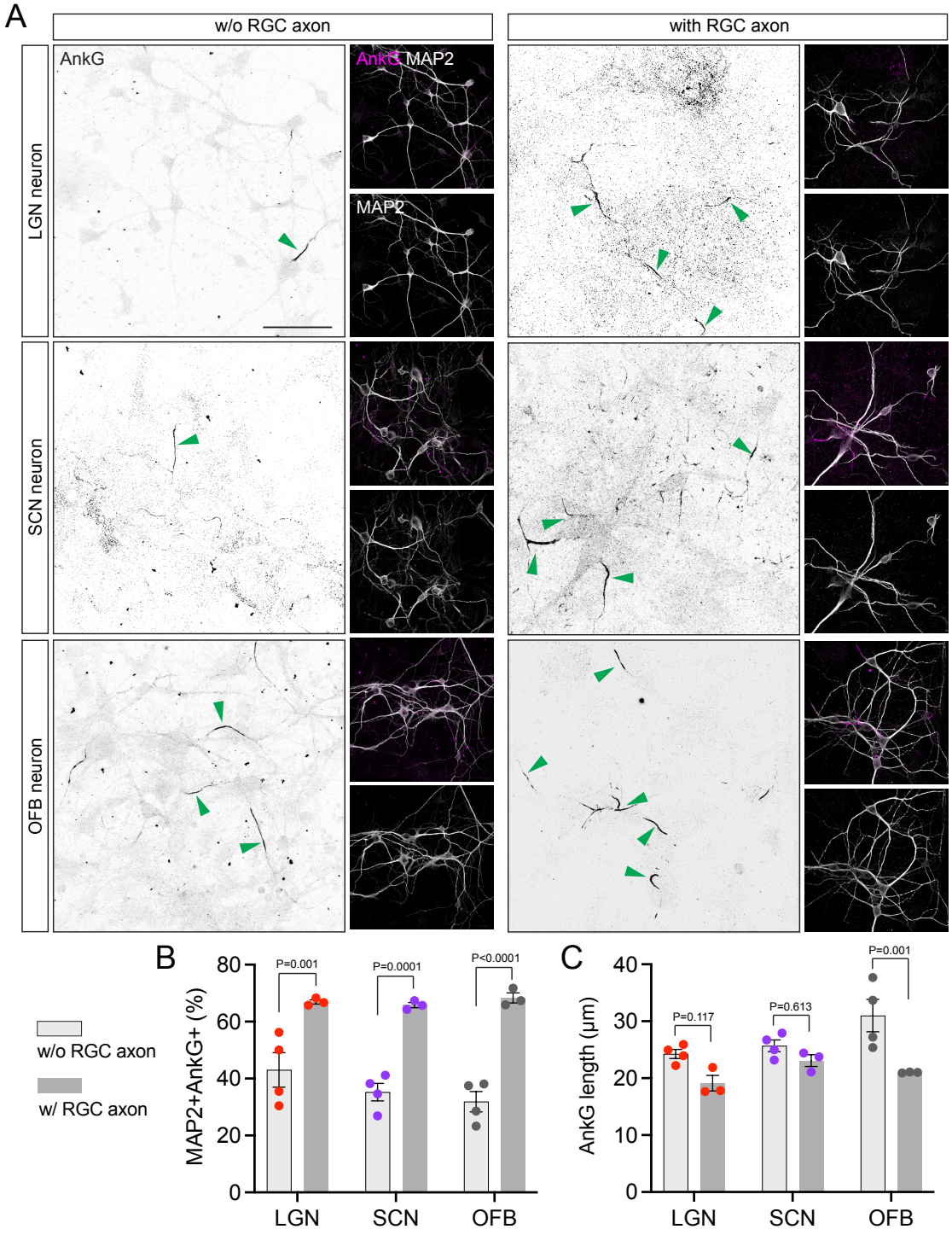
A
w/o RGC axon
with RGC axon
LGN neuron
SCN neuron
OFB neuron
AnkG
AnkG MAP2
MAP2
B
w/o RGC axon
w/ RGC axon
MAP2+AnkG+ (%)
P=0.001
P=0.0001
P<0.0001
LGN
SCN
OFB
C
AnkG length (μm)
P=0.117
P=0.613
P=0.001
LGN
SCN
OFB

Supplemental Figure 5: hRGCs promote the maturation of post-synaptic neurons in the microfluidics system. A-C. Representative low magnification and high magnification images of lateral geniculate nucleus (LGN), superchiasmatic nucleus (SCN), or olfactory bulb (OFB) post-synaptic neurons plated in the microfluidics system grown in the absence and presence of hRGC axons following staining with the axonal initial segment structural protein AnkG (black/magenta) and the dendrite marker MAP2 (white). In each case, the presence of hRGC axons promoted the formation of additional AISs (green arrows). Scale bars = 50 µm. **B-C**. The number of postsynaptic neurons (MAP2+ cells) that contained an AIS (AnkG+) was significantly increased in all three target populations where neurons were cultured in the presence of pre-syanptic hRGC axons (**B**), while only OFB neurons showed a significantly longer AIS (**C**). n = 3 to 4 biological replicates. At least 4 images were used to quantify each replicate, and the number of hRGCs quantified was greater than 30 for each condition.